



UvA-DARE (Digital Academic Repository)

Thermonuclear explosion of a massive hybrid HeCO white dwarf triggered by a He detonation on a companion

Pakmor, R.; Zenati, Y.; Perets, H.B.; Toonen, S.

DOI

[10.1093/mnras/stab686](https://doi.org/10.1093/mnras/stab686)

Publication date

2021

Document Version

Final published version

Published in

Monthly Notices of the Royal Astronomical Society

[Link to publication](#)

Citation for published version (APA):

Pakmor, R., Zenati, Y., Perets, H. B., & Toonen, S. (2021). Thermonuclear explosion of a massive hybrid HeCO white dwarf triggered by a He detonation on a companion. *Monthly Notices of the Royal Astronomical Society*, 503(4), 4734-4747. <https://doi.org/10.1093/mnras/stab686>

General rights

It is not permitted to download or to forward/distribute the text or part of it without the consent of the author(s) and/or copyright holder(s), other than for strictly personal, individual use, unless the work is under an open content license (like Creative Commons).

Disclaimer/Complaints regulations

If you believe that digital publication of certain material infringes any of your rights or (privacy) interests, please let the Library know, stating your reasons. In case of a legitimate complaint, the Library will make the material inaccessible and/or remove it from the website. Please Ask the Library: <https://uba.uva.nl/en/contact>, or a letter to: Library of the University of Amsterdam, Secretariat, Singel 425, 1012 WP Amsterdam, The Netherlands. You will be contacted as soon as possible.

UvA-DARE is a service provided by the library of the University of Amsterdam (<https://dare.uva.nl>)

Thermonuclear explosion of a massive hybrid HeCO white dwarf triggered by a He detonation on a companion

R. Pakmor¹,^{*} Y. Zenati,² H. B. Perets² and S. Toonen^{3,4}

¹Max-Planck-Institut für Astrophysik, Karl-Schwarzschild-Str 1, D-85748 Garching, Germany

²Physics Department, Technion – Israel Institute of Technology, Haifa 3200004, Israel

³Institute of Gravitational Wave Astronomy, School of Physics and Astronomy, University of Birmingham, Birmingham B15 2TT, UK

⁴Anton Pannekoek Institute for Astronomy, University of Amsterdam, NL-1090 GE Amsterdam, the Netherlands

Accepted 2021 March 3. Received 2021 February 5; in original form 2020 October 30

ABSTRACT

Normal type Ia supernovae (SNe) are thought to arise from the thermonuclear explosion of massive ($>0.8 M_{\odot}$) carbon–oxygen white dwarfs (WDs), although the exact mechanism is debated. In some models, helium accretion on to a carbon–oxygen (CO) WD from a companion was suggested to dynamically trigger a detonation of the accreted helium shell. The helium detonation then produces a shock that after converging on itself close to the core of the CO WD, triggers a secondary carbon detonation, and gives rise to an energetic explosion. However, most studies of such scenarios have been done in one or two dimensions, and/or did not consider self-consistent models for the accretion and the He donor. Here, we make use of detailed 3D simulation to study the interaction of a He-rich hybrid $0.69 M_{\odot}$ HeCO WD with a more massive $0.8 M_{\odot}$ CO WD. We find that accretion from the hybrid WD on to the CO WD gives rise to a helium detonation. However, the helium detonation does not trigger a carbon detonation in the CO WD. Instead, the helium detonation burns through the accretion stream to also burn the helium shell of the donor hybrid HeCO WD. The detonation of its massive helium shell then compresses its CO core, and triggers its detonation and full destruction. The explosion gives rise to a faint, likely highly reddened transient, potentially observable by the Vera Rubin survey, and the high-velocity ($\sim 1000 \text{ km s}^{-1}$) ejection of the heated surviving CO WD companion. Pending on uncertainties in stellar evolution, we estimate the rate of such transient to be up to ~ 10 per cent of the rate of type Ia SNe.

Key words: hydrodynamics – supernovae: general – binaries: close – nuclear reactions, nucleosynthesis, abundances – transients: supernovae.

1 INTRODUCTION

It was recently suggested that hybrid HeCO white dwarfs (WDs) might play a key role in the production of thermonuclear supernovae (SNe; Perets et al. 2019; Zenati, Toonen & Perets 2019). Their disruption by a more massive carbon–oxygen (CO) WD, and later accretion of the debris on to the CO WD was shown in 2D simulations to trigger a thermonuclear explosion of the CO WD, giving rise to a type Ia supernova. However, due to the limitations of 2D simulations, these models did not simulate the early phases of accretion from the HeCO WD on to the CO WD and the later disruption. In particular, accretion of helium from the hybrid WD on to the CO WD could potentially give rise to a dynamical detonation of the accreted helium layer (or a pre-existing helium layer on the CO WD if such exists). In such a case, it is possible that the helium layer detonation may trigger a secondary carbon detonation of the CO WD leading to its explosion, even before the companion hybrid WD is disrupted. This latter possibility follows ideas of double-detonation models beginning in the 1980s (Iben & Tutukov 1985; Iben et al. 1987), and their more recent incarnation as dynamical double detonations (see

e.g. Guillochon et al. 2010; Pakmor et al. 2013; Sato et al. 2015; Shen et al. 2018b).

In order to understand the outcomes of a CO–HeCO double degenerate binary system, and explore whether it gives rise to the disruption of the HeCO WD, we employ dynamical 3D simulations that begin following the final phase of the inspiral of the binary CO–HeCO WD system.

We specifically investigate the fate of a double degenerate binary system consisting of a primary pure CO WD with a mass of $0.8 M_{\odot}$ and a secondary hybrid HeCO WD with total mass of $0.69 M_{\odot}$ made of a CO core of $0.59 M_{\odot}$ and a massive helium shell of $0.1 M_{\odot}$. Note that both the mass ratio, and the highly He-enriched HeCO WD differ from those studied in 2D accretion disc simulations (Perets et al. 2019). In particular, the much higher He shell for this hybrid is attained through somewhat different evolution than that described in Zenati et al. (2019), as we further discuss in Section 2 below.

We obtain the density profile and composition of both WDs using the 1D stellar evolution code MESA (Paxton et al. 2011, 2019) similarly to Zenati et al. (2019). We follow the evolution of the hybrid WD starting from the main sequence as a $4.1 M_{\odot}$ star in a binary system with a separation of $a = 4.18 \text{ au}$ with a more massive $7.5 M_{\odot}$ companion star that will become the primary WD, and adopt solar metallicity $Z = Z_{\odot} = 0.02$. We discuss the formation of the double degenerate binary system in detail in Sections 2 and 6.

* E-mail: rpakmor@mpa-garching.mpg.de

Starting from the 1D profiles we then generate 3D representations of these WDs in the moving mesh hydrodynamics code AREPO (Springel 2010; Pakmor et al. 2016) that includes a fully coupled nuclear reaction network. We initialize the binary system with an initial separation of 4×10^4 km. We follow the inspiral of the binary system as the secondary hybrid WD fills its Roche lobe and transfers material to the primary WD. Eventually a detonation ignites on the surface of the primary WD in its accreted helium shell. We describe the inspiral phase and ignition of the helium detonation in Section 3.

The helium detonation sweeps around the primary CO WD and sends a shock wave into its centre. As there is not a lot of helium around the primary WD, the detonation is weak. Its shock wave still converges at the edge of the CO core of the primary WD but fails to detonate carbon. In contrast, at the same time the helium detonation propagates upwards through the dense accretion stream towards the secondary hybrid WD. When it arrives there the helium detonation also travels around the hybrid WD, burning its massive helium shell. Here, the detonation is strong and fast and its shock wave converges close to the centre of the hybrid WD where it manages to ignite the CO core. The emerging carbon detonation then burns and unbinds the whole secondary WD. We describe this phase and characterize the ejecta of the secondary hybrid WD and the properties of the surviving primary CO WD in Section 4.

We then employ the radiation transfer code SUPERNU (Wollaeger et al. 2013; Wollaeger & van Rossum 2014) to compute synthetic light curves for the explosion in Section 5. We use population synthesis to estimate the frequency of similar events and discuss the observability of the explosion and the surviving WDs in Section 6.

We finally summarize our results and provide an outlook on the most important questions that arise from our work in Section 7.

2 FORMATION OF THE BINARY SYSTEM

At the current age of the Universe, single star evolution has produced CO WDs in the mass range ~ 0.50 – $1.05 M_{\odot}$ and oxygen–neon (ONe) WDs in the mass range ~ 1.05 – $1.38 M_{\odot}$. However, binary evolution makes this picture much more complex and can give rise to WDs with very different properties including very low mass (VLM) WDs (Istrate et al. 2016; Zhang et al. 2018). Moreover, there are two ways how binary systems can produce hybrid WDs with a CO core and an outer helium shell, either through a phase of mass transfer via Roche lobe overflow (RLOF) or through a common envelope phase (see e.g. Ivanova et al. 2013).

During this binary interaction, the hydrogen-rich envelope of the star that will become the hybrid WD is stripped following the formation of a He core. The later evolution of the stripped star and its helium core is then significantly altered compared to the uninterrupted evolution of an identical but non-interacting (single) star. After most of the red giant envelope is removed the outer hydrogen shell burning is quelled, but the helium-core keeps growing in mass (Prada Moroni & Straniero 2009), and the star begins to contract. If the helium core is sufficiently massive, the contraction will eventually trigger helium ignition (Iben & Tutukov 1985; Zenati et al. 2019) and the formation of a CO core. In this case, the helium to CO abundance ratio of the final WD will be determined by the specific detailed evolution of helium burning as well as mass-loss through winds from the envelope (Tutukov & Yungelson 1992; Prada Moroni & Straniero 2009; Zenati et al. 2019).

As shown in Zenati et al. (2019) such interacting binary systems can produce hybrid WDs in the mass range of 0.38 – $0.72 M_{\odot}$ with a helium envelope containing ~ 2 – 20 per cent of the total mass of the WD. Recent observational evidence for the existence of such

hybrid WDs has been mounting. The ZTF survey (Kupfer et al. 2020) reported their finding of the first short-period binary in which a hot subdwarf star (sdOB) has filled its Roche lobe and has started mass transfer to its companion. The binary system has a period of $P = 39.3401$ min, making it the most compact hot subdwarf binary currently known. Kupfer et al. (2020) estimated that the hot subdwarf will become a hybrid WD (with a helium layer of $\sim 0.1 M_{\odot}$) and merge with its CO WD companion in about 17 Myr. In this case, it may end in a thermonuclear explosion or form an R CrB star. In addition, Beuermann et al. (2020) and Parsons et al. (2020) found eclipsing binaries that may have a hybrid WD as their primary star.

2.1 A highly He-enriched hybrid WD

In this work, we explore the fate of a close binary system consisting of a $0.8 M_{\odot}$ CO WD and a $0.69 M_{\odot}$ hybrid WD that has a helium shell with a mass of $0.1 M_{\odot}$ or ~ 14 per cent of its mass. Although this hybrid WD is produced through the same stellar evolution stages as the hybrid WD of the same total mass in Zenati et al. (2019), some different choices of parameters give rise to a more He-enriched WD than those described in Zenati et al. (2019). We follow the stellar evolutionary tracks of both binary components from the pre-main-sequence stage to the final binary system consisting of two WDs. We stop the evolution once the star becomes a fully degenerate WD. This condition effectively translates to a WD luminosity and temperature below $L \leq 1.12 L_{\odot}$ and $T_{\text{eff}} \leq 4.92 T_{\odot, \text{eff}}$, respectively.

The evolution of the binary system depends strongly on the initial conditions. Based on our population modelling, we describe the typical binary evolution in Section 6. It is important to note that the initial conditions of the binary system studied here are different than those described in Zenati et al. (2019) for the formation of the $0.69 M_{\odot}$ HeCO WD. Here, we begin with an initial mass ratio $q = M_{\text{donor}}/M_{\text{companion}} \sim 0.58$ and an initial orbital period $P = 4.37$ d. We also consider slightly different overshooting parameter (0.0012) and mixing parameter ($\alpha = 1.3$).

We explored a range of hybrid WDs to choose the parameters and found these parameters give rise to very similar results for WDs less massive than $0.63 M_{\odot}$ as described in Zenati et al. (2019). However, when considering these parameters for the formation of more massive hybrids, they give rise to the formation of an even more He-enriched HeCO WD than discussed in Zenati et al. (2019), such as the one considered here. These results will be discussed in depth in a dedicated paper.

3 INSPIRAL AND IGNITION

Once a binary system with two WD components has formed, it slowly loses angular momentum via gravitational wave emission until eventually the two WDs get sufficiently close for the secondary (hybrid) WD to fill its Roche lobe. It then starts transferring mass on to the primary CO WD. For a long time, mass transfer is very slow and irrelevant for the properties of the system, while the orbit continues to shrink from further emission of gravitational waves, and the mass transfer rate increases. Eventually the binary becomes sufficiently close such that the mass transfer rate is large enough as to transfer substantial amounts of mass on a time-scale of several orbits. At this point, which serves as the initial starting point of our 3D simulation, the density of the accretion stream continues to increase, and unless interrupted by other process would eventually lead to the disruption of the secondary, after a few tens of orbits. However, we find that in the configuration explored here,

thermonuclear detonation occurs beforehand, and gives rise to very different outcomes, as we now describe.

3.1 AREPO

To model the dynamical evolution of the binary system, we use the moving-mesh code AREPO (Springel 2010; Pakmor et al. 2016; Weinberger, Springel & Pakmor 2020). It discretizes the volume into cells and solves the equations of hydrodynamics using a second-order finite-volume scheme (Pakmor et al. 2016). Its Voronoi mesh is reconstructed in every time-step from a set of mesh-generating points that each span up single cell. Fluxes over interfaces are computed using the HLLC Riemann solver in the moving frame of the interface (Pakmor, Bauer & Springel 2011). We use AREPO in its pseudo-Lagrangian mode, i.e. the mesh-generating points follow the gas velocity with small corrections to keep the mesh regular. On top of the movement of the mesh-generating points, we employ explicit refinement and de-refinement for cells that are more than a factor of two away from the desired target gas mass of the cells. For the simulation presented here, our target mass resolution is always $m_{\text{target}} = 10^{-7} M_{\odot}$. In addition, we require that the volume of a cell is not more than 10 times larger than its largest direct neighbour, otherwise the cell is refined.

In addition to hydrodynamics, AREPO includes self-gravity of the gas. Gravitational accelerations are computed using a tree solver and are coupled to the hydrodynamics via a Leapfrog time-integration scheme. The gravitational softening of the cells is set to be equal to 2.8 times their radius, with a minimum softening of 10 km. To improve the efficiency of the simulation we use local time-steps in AREPO, i.e. every cell is integrated on the largest time-step of a discrete set of time-steps, that is smaller than the time-step of its local time-step criteria. This way only a small number of cells is integrated on the smallest time-step in the simulation and the bulk of the cells can be integrated on much larger time-steps.

To model degenerate electron gases present in WDs, we use the HELMHOLTZ equation of state (Timmes & Swesty 2000) including Coulomb corrections. Moreover, we include a 55 isotope nuclear reaction network fully coupled to the hydrodynamics (Pakmor et al. 2012). The included isotopes are n, p, ^4He , ^{11}B , $^{12-13}\text{C}$, $^{13-15}\text{N}$, $^{15-17}\text{O}$, ^{18}F , $^{19-22}\text{Ne}$, $^{22-23}\text{Na}$, $^{23-26}\text{Mg}$, $^{25-27}\text{Al}$, $^{28-30}\text{Si}$, $^{29-31}\text{P}$, $^{31-33}\text{S}$, $^{33-35}\text{Cl}$, $^{36-39}\text{Ar}$, ^{39}K , ^{40}Ca , ^{43}Sc , ^{44}Ti , ^{47}V , ^{48}Cr , ^{51}Mn , $^{52, 56}\text{Fe}$, ^{55}Co , and $^{56, 58-59}\text{Ni}$. We use the JINA reaction rates (Cyburt et al. 2010). Nuclear reactions are computed for all cells with $T > 10^6$ K except for cells that are part of the shock front that we assume to be the case when $\nabla \cdot \vec{v} < 0$ and $|\nabla P| r_{\text{cell}}/P > 0.66$ (Seitenzahl et al. 2009). Note that we reran the simulation until the nuclear burning ceases with an additional limiter that artificially reduces nuclear reaction rates to guarantee that the nuclear time-scale is always longer than the hydrodynamical time-step of a cell (Kushnir et al. 2013; Shen et al. 2018a). As we show and discuss in Appendix A, the results are essentially identical, with the main difference that the helium detonation moves slower with the additional limiter that reduces the reaction rates.

3.2 Set-up and inspiral

From the stellar evolution calculation, we obtain the density profile, temperature profile, and composition profile of both WDs. To generate the 3D initial conditions in AREPO, we employ a healpix-based algorithm that generates roughly cubical initial cells (Pakmor et al. 2012; Ohlmann et al. 2017). We first put both stars individually into a box with boxsize 10^5 km with a background density of 10^{-5} g cm $^{-3}$

and background specific thermal energy of 10^{14} erg g $^{-1}$. We relax them for 40 s (for the $0.8 M_{\odot}$ CO WD) and 60 s (for the $0.69 M_{\odot}$ hybrid WD). For the first 80 per cent of the relaxation, we apply a friction force that damps out initial velocities that are introduced from noise in the original mesh. In the last 20 per cent of the relaxation time, we disable the friction force and check that the density profiles of the WDs do not change anymore, i.e. that the relaxed stars are stable at their initial profile.

After the relaxation, we take the final state of both WDs from their relaxation in isolation and add them together into a simulation box with a size of 10^7 km. We put the WDs on a spherical co-rotating orbit at a distance of $a = 4.2 \times 10^4$ km, which sets the initial orbital period to $T = 120$ s. We chose this initial orbit rather wide so that the initial tidal forces of the WDs on each other are small. We use a passive tracer fluid to track the material of each WD individually in the simulation. This also allows us to easily compute the centres of both WDs.

At this separation gravitational wave inspiral is still relevant, though it takes too much time to follow the system with its true inspiral rate. To circumvent this problem, we add a tidal force that removes angular momentum from the binary system similar to gravitational waves. However, we chose the force such that the separation a decreases at a constant rate v_a , i.e.

$$\frac{da}{dt} = v_a. \quad (1)$$

This leads to a purely azimuthal acceleration on the primary WD given by

$$\vec{a}_1 = -\frac{M_2^2}{M_1 + M_2} \frac{G}{2a} \frac{\vec{v}_1}{v_1^2} v_a, \quad (2)$$

and vice versa for the secondary WD. We chose $v_a = 50$ km s $^{-1}$ so that the orbit changes fast compared to physical gravitational wave emission but slowly compared to the dynamical time-scales of the WDs so that the WDs can easily adapt to the changing tidal forces.

The evolution of the orbits of the two WDs is shown in Fig. 1. At $t = 430$ s, after about six orbits, the orbital period has decreased to $T = 38$ s and the separation to $a = 1.9 \times 10^4$ km. At this point, we switch off the angular momentum loss term. The point where it is switched off is chosen such that the accretion stream is dense enough to dynamically affect the surface of the primary WD.

At this time, the secondary WD has donated $4 \times 10^{-3} M_{\odot}$ of helium to the primary WD that now forms a helium shell on the surface of the primary WD. Moreover, about $4 \times 10^{-5} M_{\odot}$ of pure helium material has been unbound from the system through tidal tails.

3.3 Ignition of the helium detonation

A density slice through the mid-plane of the binary system is shown in top row of Fig. 2 when the system has evolved 10 s past the point when we switched off the angular momentum loss term. As the accretion stream shears along the surface of the primary CO WD, it generates Kelvin–Helmholtz instabilities that disturb the initially separated helium and carbon–oxygen layers. At this time, the accreted helium layer and the CO core of the primary WD have mixed only very little.

A zoom-in on this interface (additional rows in Fig. 2) shows the base of one helium-rich bubble on the surface of the primary CO WD with a radius of about 10^3 km. The gas here is compressed and heated up and eventually reaches a temperature of about 10^9 K at a density larger than 2×10^5 g cm $^{-3}$. The cells in this hotspot have a typical radius of 15 km. Under these conditions, helium starts to burn

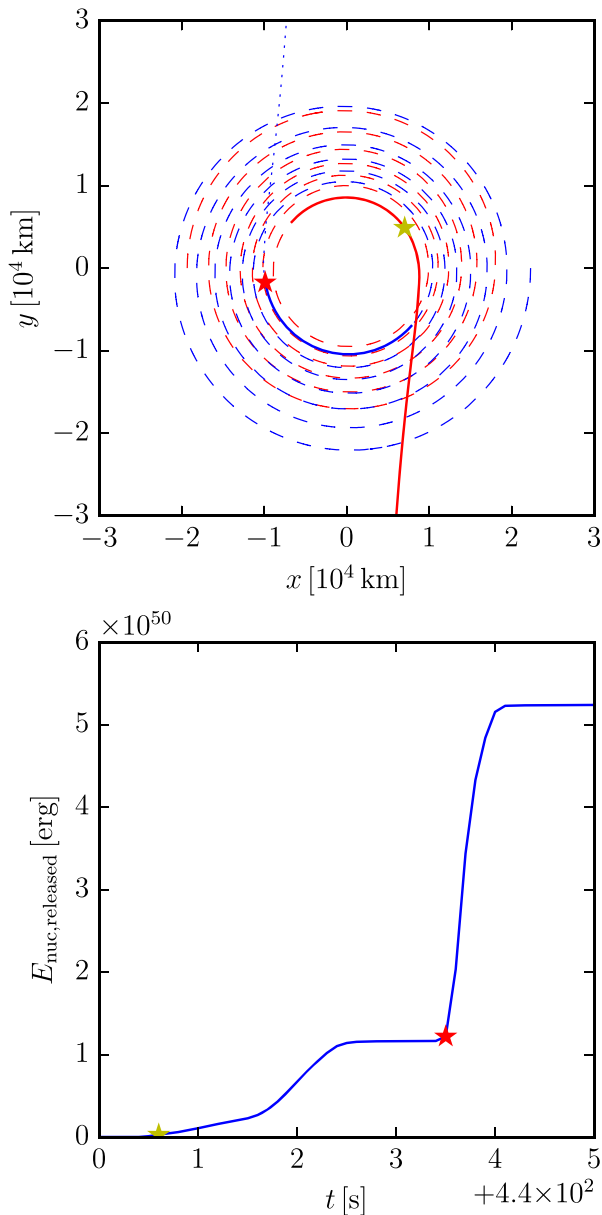


Figure 1. The top panel shows the orbital evolution of the two WDs in the binary system in the plane of rotation. Dashed lines show their path while the additional force mimicking gravitational wave emission is active. Straight lines show the evolution of the primary WD (red) and the secondary WD (blue). The latter ends when the secondary WD is disrupted. The yellow star denotes the moment when the helium detonation ignites first on the surface of the primary WD. The red star marks the time when the carbon detonation ignites in the centre of the secondary WD after which it is quickly disrupted. The blue dotted line shows the movement of the centre of mass of the ejecta of the secondary WD. The lower panel shows the cumulative total nuclear energy released. Stars again mark the ignition of the helium detonation (yellow) and the carbon detonation (red).

explosively and a helium detonation forms quickly, consistent with ignition simulations of resolved helium detonations (Shen & Moore 2014). The helium is burned to intermediate mass elements. The helium detonation compresses the material as the shock runs over it and heats it up as shown in the right-hand panel of the second row of

Fig. 2. Note that the helium detonation forms at the same place when the additional burning limiter is applied (for details, see Appendix A).

The temperatures and densities of the burning helium layers are not sufficiently hot or dense enough to also burn the adjacent pure CO material, so the helium detonation first propagates outwards into the helium shell of the primary WD and then starts sweeping around it. At the same time, the helium detonation sends a shock wave into the CO core of the primary WD. A summary of the global properties of the detonation is shown in Table 1.

4 EXPLOSION

After the formation of the helium detonation the situation is initially similar to the well-known double detonation scenario (Fink, Hillebrandt & Röpke 2007; Guillochon et al. 2010; Pakmor et al. 2013), in which the helium detonation travels around the primary WD while sending a shock wave into the carbon–oxygen core. In this scenario, the eventually spherical shock wave converges in a single point in the core where it ignites a carbon detonation that disrupts the WD.

The main difference to the system we investigate here is that the helium detonation does not detonate our primary WD, but detonates the secondary WD instead. Moreover, the secondary WD produces radioactive ^{56}Ni despite its low mass as it is strongly compressed prior to its explosion.

Since the helium detonation will travel all around the primary WD, it is unavoidable that the shock wave that it sends into the CO core will eventually converge at a single point. The strength of the shock, the position of this point, and most importantly the gas density at the convergence point will decide if a carbon detonation forms. The position of the convergence point depends on the speed of the shock wave that is moving through the CO core relative to the speed of the helium detonation moving around the core and the size of the core relative to the circumference of the CO core.

If the helium detonation is much faster than the shock wave it generates at the surface that is travelling into the core, the shock wave starts roughly at the same time everywhere on the surface. In this case, the convergence point is close to the centre of the core. In contrast, if the helium detonation is comparable in speed or slower than the shock wave that is propagating into the core, the convergence point will be close to the interface between the helium shell and CO core opposite to the ignition point of the helium detonation.

Therefore, the position of the convergence point depends fundamentally on the properties of the helium shell and the CO core of the WD. In particular, a higher density at the base of the helium shell increases the speed and completeness of the nuclear burning and the helium detonation becomes stronger and faster, and also sends a stronger shock into the core. As a rule of thumb, if the shock wave converges in the CO core at a density $\geq 10^7 \text{ g cm}^{-3}$ a carbon detonation will likely form, while carbon burning will likely not start if the density is below $3 \times 10^6 \text{ g cm}^{-3}$ (Seitenzahl et al. 2009; Shen & Bildsten 2014).

4.1 Primary WD

Our primary WD is significantly less massive (only $0.8 M_{\odot}$) than the WDs typically studied in attempts to make type Ia supernovae, which require roughly solar mass primary WDs (Sim et al. 2010; Shen et al. 2018a). Note also that the central density of our pre-shocked primary WD barely reaches 10^7 g cm^{-3} , below which a carbon detonation does not produce any radioactive ^{56}Ni .

The propagation of the detonation in the helium shell around the primary WD and through its CO core is shown in Fig. 3. It takes the

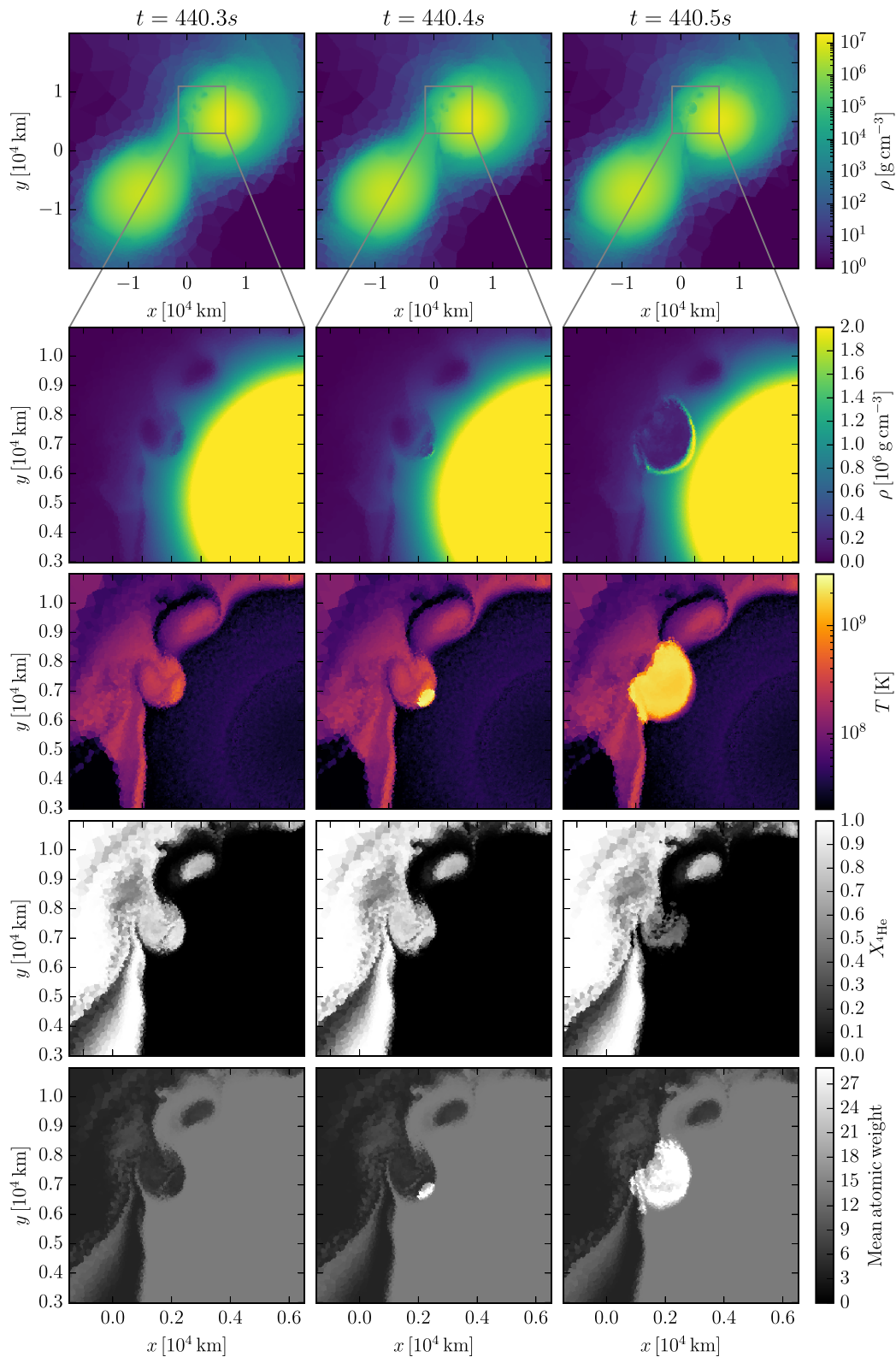


Figure 2. Columns show slices through the mid-plane of the binary for the snapshots just before, at, and directly after the formation of the first detonation, the helium detonation on the surface of the primary CO WD. The snapshots are separated by 0.1 s. The top row shows a density slice of the whole binary, the bottom rows show slices zooming in on the position where the detonation forms featuring density, temperature, mass fraction of ${}^4\text{He}$, and mean atomic weight, respectively.

Table 1. Physical conditions that lead to ignition of the helium and carbon detonations and their global yields. The table shows the ignition temperature, ignition density, and ignition time of the detonations as well as the total energy release and the amount of intermediate mass elements and iron group elements that the detonation synthesises.

Event	T_{ign} (K)	ρ_{ign} (g cm^{-3})	t_{ign} (s)	ΔQ_{nuc} (erg)	IME (M_{\odot})	IGE (M_{\odot})
He det	2.2×10^9	2×10^5	440.5	1.2×10^{50}	4.7×10^{-2}	3.5×10^{-3}
C det	3.8×10^9	2×10^7	443.5	4×10^{50}	3.4×10^{-1}	2.3×10^{-2}

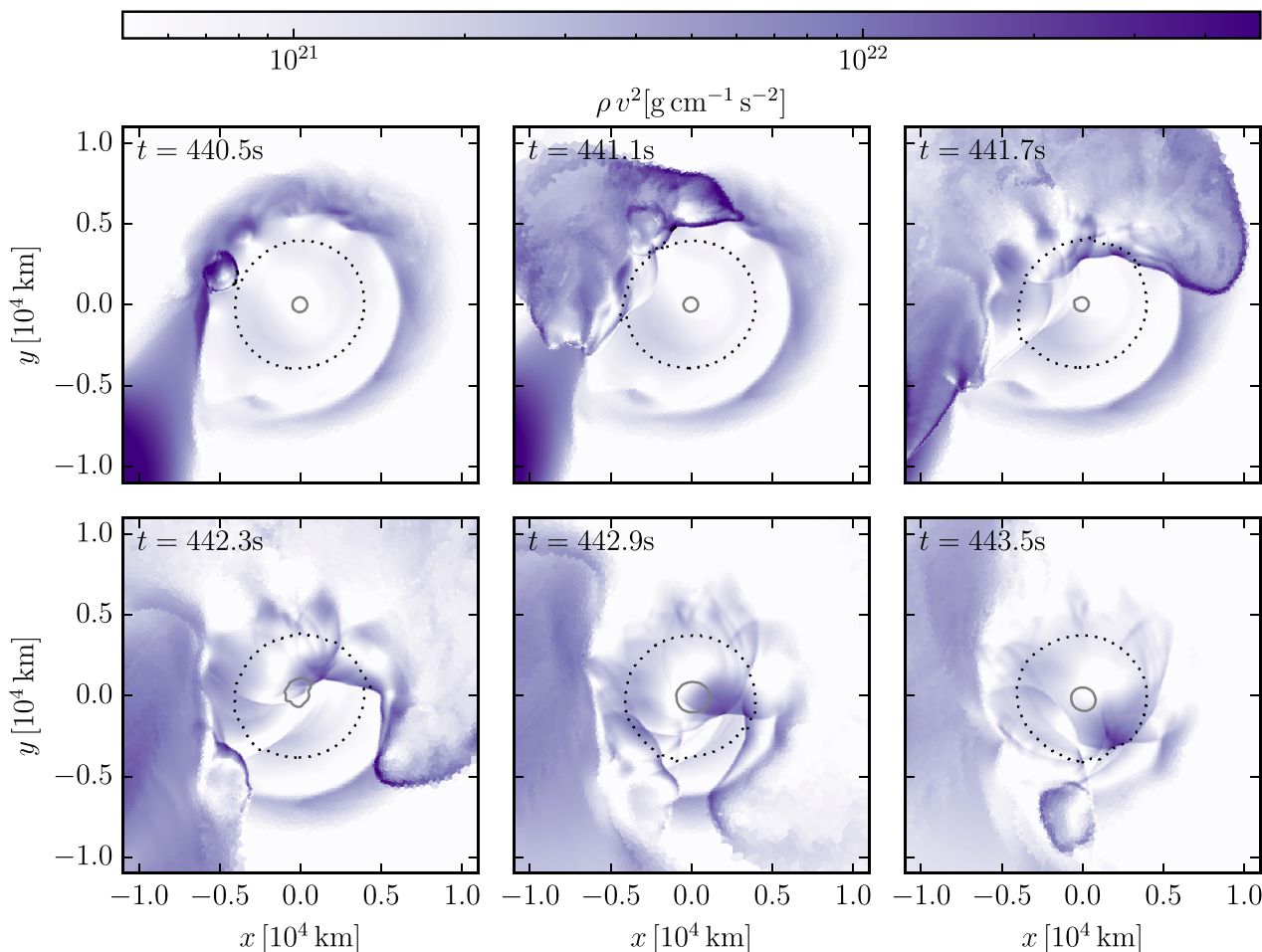


Figure 3. Propagation of the shock originating from the helium detonation as it moves around the primary WD. The panels show the time evolution from the time of the ignition of the helium detonation (top left panel) to the time when the shock converges in the CO core of the primary WD (bottom right panel). The black dotted and grey solid contours indicate densities of 2×10^6 and 10^7 g cm^{-3} , respectively.

helium detonation about 3 s to reach the opposite side of the point of ignition. In this time, it releases 2×10^{49} erg from burning the helium shell around the primary WD.

The shock wave it sends into the CO core compresses the core only marginally, temporarily increasing its central density by ≈ 5 per cent from 1.03×10^7 to $1.08 \times 10^7 \text{ g cm}^{-3}$.

The shock wave takes about the same time to cross the core as the helium detonation to burn around the core, so that the detonation converges roughly at the edge of the CO core at the opposite side of the ignition of the helium detonation. The shock convergence occurs far off-centre at a radius of about 5000 km and at a density of only $\approx 2 \times 10^6 \text{ g cm}^{-3}$. Owing to the low density and the weak detonation the converging shock fails to ignite a carbon detonation. It is possible that with significantly higher resolution a carbon detonation might

form, though the conditions are probably just insufficient as far as we can tell from resolved 1D ignition simulations (Seitenzahl et al. 2009; Shen & Bildsten 2014). Note that creating a carbon detonation also fails with an additional burning limiter (for details see Appendix A), so we are reasonably confident that this result does not depend on the details of the numerical treatment of the detonation.

Compared to Pakmor et al. (2013) who simulated a system with a similar primary WD of $1.0 M_{\odot}$ with a helium shell of $0.01 M_{\odot}$ our primary WD in this simulation is less massive, so the central density as well as the density at the base of the helium shell are lower. Therefore, the nuclear burning in the helium detonation is less complete, it releases less energy, and the helium detonation is weaker and slower. For comparison, the helium detonation only

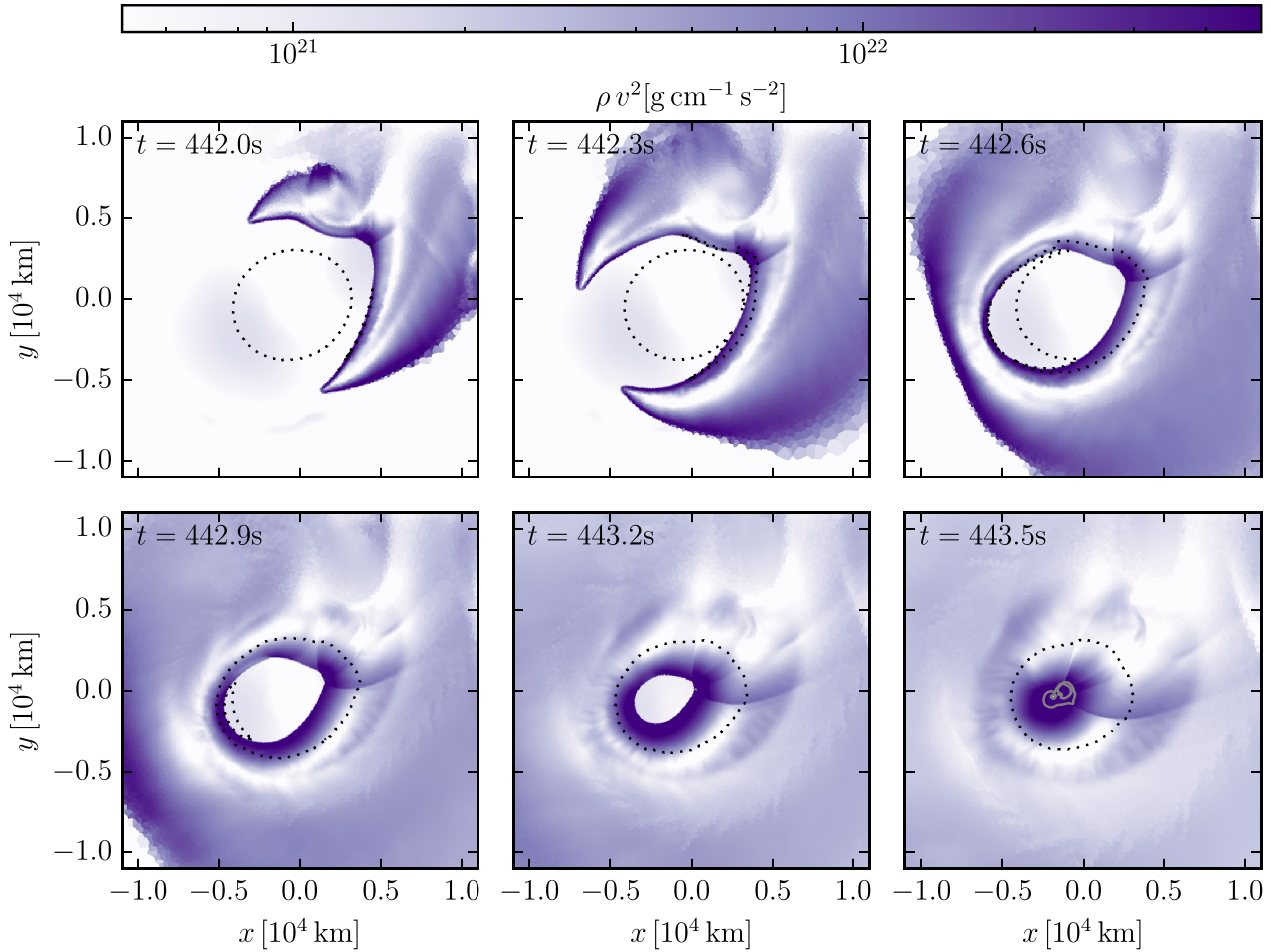


Figure 4. Propagation of the shock originating from the helium detonation moves around the secondary WD. The panels show the time evolution from the time when the helium detonation arrives at the secondary WD and starts to propagate around it (top left panel) to the time when the shock converges in the carbon-oxygen core of the secondary WD (bottom right panel). The black dotted and grey solid contours indicate densities of 2×10^6 and 10^7 g cm^{-3} , respectively.

needs 1 s to travel around the $1.0 M_{\odot}$ primary WD in Pakmor et al. (2013) compared to 3 s for our $0.8 M_{\odot}$ primary WD.

One way to improve the chances of creating a carbon detonation may be to increase the strength of the helium detonation, through the existence of a larger He-shell mass. Higher mass could possibly be mediated by a longer period of mass transfer from the secondary hybrid WD to the primary CO WD prior to the dynamical interaction between both WDs that we model here. For this, the binary system probably needs to transfer several $0.01 M_{\odot}$ of helium to the primary WD during the many orbits in which the secondary WD already fills its Roche lobe but when the accretion rates are very low and the accretion is dynamically unimportant. Whether such a scenario is possible is unknown as, unfortunately, it is not feasible at the moment to properly simulate such a system for the millions of orbits that would be required to model this phase properly. If such a scenario works its rates could be non-negligible (Ruiter et al. 2014). Moreover, the primary CO WD could also have obtained a He-shell during the evolution of the binary system (Neunteufel, Yoon & Langer 2016, 2019).

4.2 Secondary WD

The main difference in our system compared to previous simulations (see e.g. Pakmor et al. 2013) is the hybrid nature of the secondary

WD, which has a massive helium shell but is more massive than a pure helium WD and has a much higher central density. As we show, this difference gives rise to qualitatively different evolution and outcomes that previous models where He WD secondaries were considered.

At the time the helium detonation ignites on the primary, the accretion stream from the secondary WD to the primary WD consists mostly of helium and is degenerate with a density of about 10^5 g cm^{-3} . When the helium detonation that is sweeping around the primary WD reaches the end of the accretion stream, it is able to travel upwards through the accretion stream and reach into the helium shell of the hybrid WD. Note that the total mass in the accretion stream is small so its energy release is negligible compared to the helium burned on the surface of the two WDs.

The propagation of the helium detonation around the secondary WD and the shock it sends into its CO core is shown in Fig. 4. Since most of the original $0.1 M_{\odot}$ of helium is still on the secondary WD and the base of the helium shell is at a comparably high density of $\sim 10^6 \text{ g cm}^{-3}$, the helium detonation on the secondary WD is very energetic and fast. It sweeps around it in less than 0.5 s, much faster than the shock wave it sends into the CO core of the secondary WD and releases 1.0×10^{50} erg of energy from burning the helium shell around the secondary WD, about five times the amount released from burning the helium shell around the primary WD.

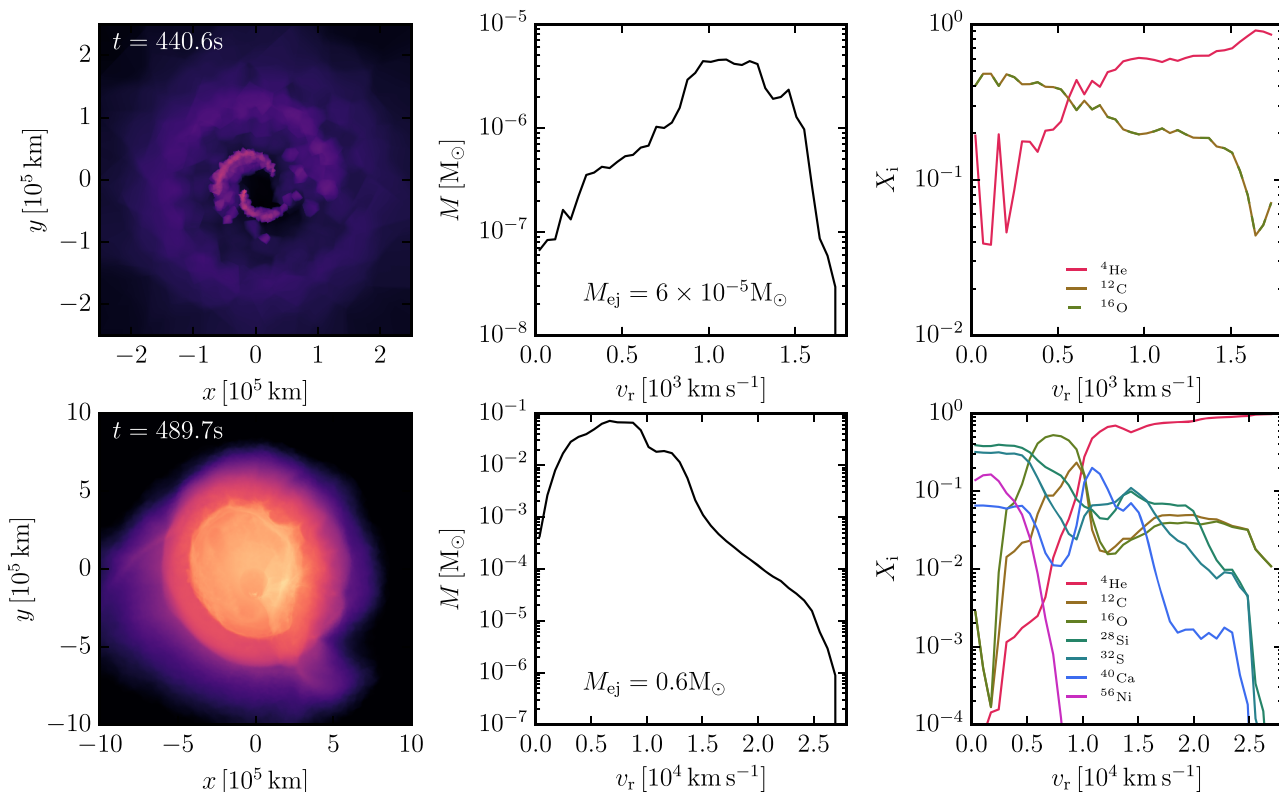


Figure 5. Unbound ejecta at the time of the ignition of the helium detonation on the surface of the CO WD (top row) and at the end of the simulation long after the carbon detonation. The left-hand panels show the projected density of the unbound material. The middle and right-hand panels show the distribution of the mass of the ejecta (middle panel) and composition (right-hand panel) in velocity space.

As shown in Fig. 4, the shock wave that is travelling into the core is therefore starting on an almost spherical surface. It converges about 1 s after the helium detonation around the secondary hybrid WD ceases close to its centre. As the shock wave is quite energetic, it also compresses the secondary WD in the centre prior to converging there and raises its central density significantly by almost a factor of three from 5.6×10^6 to 1.5×10^7 g cm^{-3} .

When the shock wave converges close to the centre at a density of about 10^7 g cm^{-3} , it heats up carbon enough to ignite a carbon detonation. Similar to the convergence in the primary WD, the formation of the carbon detonation happens independently of the details of the treatment of the detonation (for details see Appendix A). Once the carbon detonation has been ignited, it quickly sweeps through the CO core of the hybrid WD. It releases 4×10^{50} erg of nuclear energy and unbinds the secondary WD. Its ashes then expand and leave the intact primary WD behind.

4.3 The unbound ejecta

After the carbon detonation has burned the secondary WD completely, its hot ashes become unbound and expand. Eventually they reach homologous expansion. We show the ejecta 46 s after the ignition of the carbon detonation in the lower row of Fig. 5. At this time, the structure of the ejecta deviates only by a few per cent from homologous expansion.

The ejecta contain a total of $0.6 M_{\odot}$ that is most of the mass of the secondary WD. The mass distribution of the ejecta is similar to a low energetic type Ia supernova with most of its mass between 5000 and 10 000 km s^{-1} and a VLM tail up to 27 000 km s^{-1} . The ejecta consist

mostly of oxygen ($0.21 M_{\odot}$), silicon ($0.16 M_{\odot}$), sulphur ($0.09 M_{\odot}$), helium ($0.07 M_{\odot}$), and carbon ($0.06 M_{\odot}$). The ejecta contain only $0.02 M_{\odot}$ of iron group elements of which $0.013 M_{\odot}$ is ^{56}Ni . The small amount of iron group elements is a direct consequence of the low central density of the hybrid WD. It produced iron group elements in the carbon detonation only because it was compressed in the centre by the helium detonation prior to the ignition of the carbon detonation.

Almost all of the mass of the ejecta is at velocities $v \leq 15\,000$ km s^{-1} . The outer parts of the ejecta ($v \geq 10\,000$ km s^{-1}) are dominated by unburned helium and only have small trace contributions of carbon, oxygen, and intermediate mass elements. The core of the ejecta ($v < 5000$ km s^{-1}) is dominated by intermediate mass elements and contains all of the radioactive ^{56}Ni in the ejecta. The part in between, which contains most of the mass, is dominated by oxygen and contains significant amounts of intermediate mass elements.

We expect the remnant of this explosion to look similar to the remnant of an ordinary low-energy supernova, as it has a similar mass and kinetic energy.

In the top row of Fig. 5, we show the unbound material at the time the helium detonation ignites, i.e. before any relevant amount of nuclear burning has happened, in a similar way. This material has been ejected from the outer Lagrange point of the secondary WD and forms an outflowing spiral structure around the binary system. It mostly consists of helium and has a typical velocity of 1000 km s^{-1} with a significant tail down to a few 100 and up to 1500 km s^{-1} . Although the ejected mass is unphysically low as we only follow the binary system for a few orbits prior to the explosion, the velocity distribution provides an idea of outflowing material in the system prior to the explosion that may become visible either by interaction with the

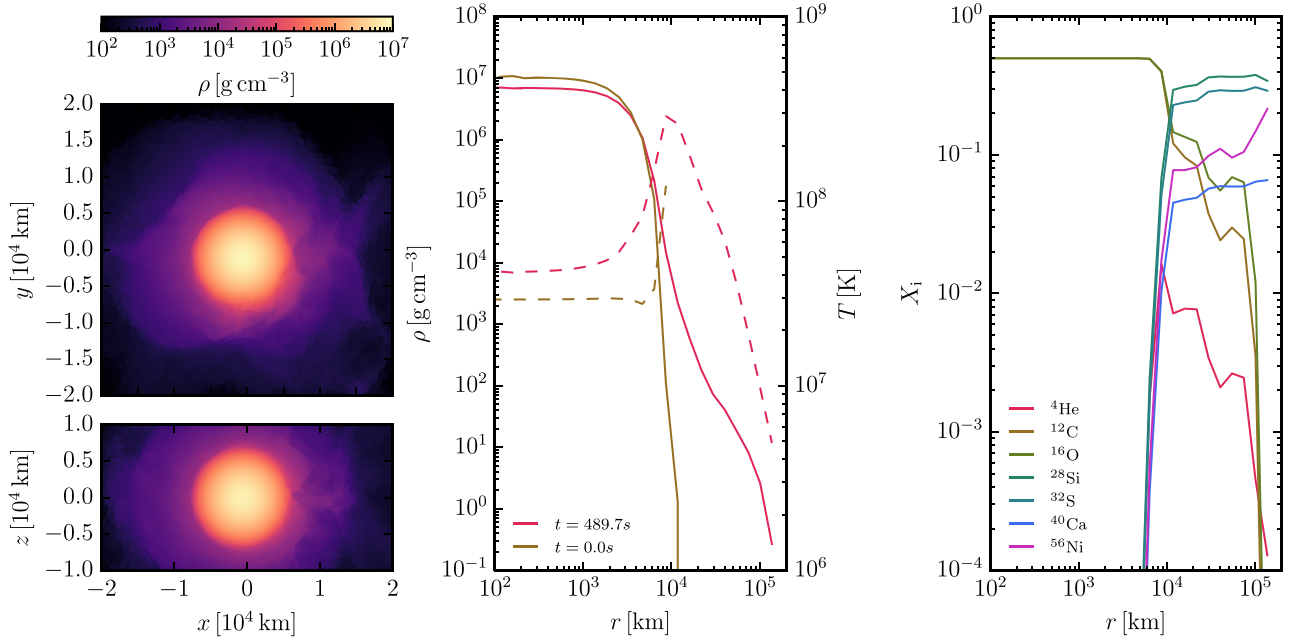


Figure 6. Surviving primary WD at the end of the simulation. The left-hand panel shows density slices in the plane of rotation and perpendicular to it. The middle panel shows the radial density (solid lines) and temperature (dashed lines) profile of the surviving WD as well as the initial density profile of the primary WD at the beginning of the simulation for comparison. The right-hand panel shows the composition of the surviving WD.

ejecta of the explosion or as early absorption lines in the supernova spectra (see e.g. discussion of CSM interaction in WD–WD mergers in Jacobson-Galán et al. 2020 and Bobrick et al. in preparation).

We present detailed synthetic light curves and spectra for the ejecta in Section 5.

Note that the ejecta in Fig. 5 are shown in their rest frame. This frame moves with a velocity of $v_{\text{kick,ejecta}} = 1600 \text{ km s}^{-1}$ relative to the rest frame of the original binary system. This relative velocity is a direct consequence of burning only one of the WDs. Its material, as it is burned, is moving with the orbital velocity of the secondary WD relative to the centre of the binary system. When the ashes of the secondary WD suddenly expand after the nuclear burning has ceased, they essentially keep their bulk velocity. Since an external observer sees the binary system and therefore also the ejecta from a random angle, we would expect that spectral lines in observed spectra of this explosion exhibit a shift between $-v_{\text{kick,ejecta}}$ and $v_{\text{kick,ejecta}}$ relative to the rest frame of its host galaxy that follows a cosine distribution. The shift is large enough to easily be detected and is a clear prediction for our system.

Note that this velocity shift is inherently expected for any explosion of a single WD in a binary system and its magnitude will be roughly equal to the orbital velocity of the exploding WD. For non-degenerate companions the orbital velocity is typically of order 100 km s^{-1} , so this shift will hardly be visible. In contrast, for a binary system of massive CO WDs (Pakmor et al. 2013; Shen et al. 2018a) a shift of order of 2000 km s^{-1} is expected that should be detectable in a sufficiently large sample of normal type Ia supernovae if their origin is dominated by such a scenario. Furthermore, if one identifies a candidate supernova remnant (SNR) from any such scenario in the galaxy, its centre of mass velocity should show such high-velocity shifts compared to its rest-frame velocity in the galaxy. Moreover, if suggested to be related with a hypervelocity WD (e.g. in one of the cases suggested by Shen et al. 2018b), the SNR centre-of-mass velocity should be in the opposite direction from that of the hyper-velocity WD.

4.4 The primary WD as surviving hyper-velocity WD

After the secondary WD suddenly explodes and its ejecta becomes unbound, the primary WD is left behind. Without its companion, it continues to move on a straight line with the orbital velocity it had at the time of the explosion. For our system, it ends up moving with a velocity of $v_{\text{kick,WD}} = 1300 \text{ km s}^{-1}$ relative to the rest frame of the original binary system.

The density profile, temperature profile, and composition profiles of the primary CO WD at the end of the simulation are shown in Fig. 6. The core of the WD is essentially undisturbed and very close to spherical for $r \leq 5000 \text{ km}$. The central density has decreased by about a factor of 2 and the central temperature has increased to about $5 \times 10^7 \text{ K}$.

At larger radii $r > 5000 \text{ km}$, the WD has changed more significantly. The helium it had accreted prior to the explosion has mostly been burned to heavier elements and became unbound, but some part of it as well as some part of the ejecta of the secondary WD have been captured by the primary WD and now constitute a large fluffy envelope. This envelope has increased the radius of the CO WD from initially $\sim 10^4 \text{ km}$ by an order of magnitude to $\sim 10^5 \text{ km}$. The envelope is quite hot with a peak temperature of $2 \times 10^8 \text{ K}$ at the base of the envelope and 10^6 K at its surface. The composition of the envelope is dominated by the intermediate mass elements with a little bit of helium. There is also a small amount of $5 \times 10^{-3} M_{\odot}$ radioactive ^{56}Ni present in the envelope.

The surviving WD is slightly more massive than the original primary CO WD. It lost $0.01 M_{\odot}$ but gained $0.04 M_{\odot}$ from the secondary hybrid WD, most of it from capturing low-velocity ejecta of its explosion.

The properties of the surviving WD are particularly interesting in light of the recently found ‘D6’ WDs that have been argued to be the surviving secondary WDs in the dynamically driven double degenerate double detonation (D6) scenario for normal type Ia supernovae (Shen et al. 2018b). These WDs appear to have a

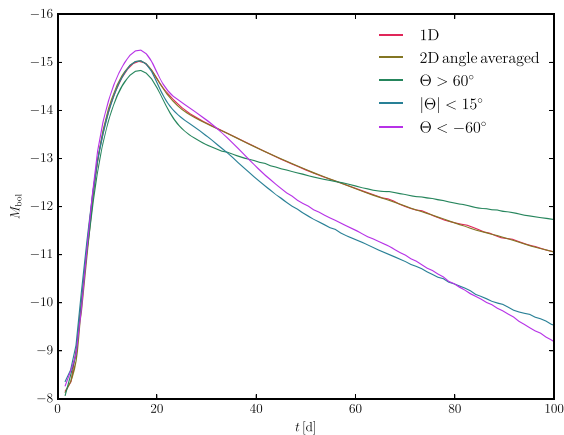


Figure 7. Bolometric light curves for the spherically symmetric 1D model (red), the angle averaged light curve of the 2D model (brown) and three different angles including both polar directions and the plane of rotation.

large fluffy envelope consisting of intermediate mass and iron group elements. They show neither hydrogen nor helium in their spectra, potentially consistent with our results of no hydrogen and at most very little (not observable) amount of helium on the surviving WD. In the D6 model, the donor WD must have had a helium envelope. Shen et al. (2018b) suggest that helium is not observed in the hyper-velocity objects because of low temperatures. It is not clear what the temperatures of the donor should be in the D6 model, but in any case we note that any helium shell might have burned following the explosion, similar to our model where the helium detonation propagates back to the donor.

The observed WDs move with a velocity of $\sim 10^3$ km relative to the Milky Way, comparable to our findings. Moreover, their number is significantly lower than what we naively expected to find if every normal type Ia supernova produces one of them, as suggested by the D6 model. These numbers, however, are potentially consistent with the rates we infer. We will discuss this connection further in Section 6 where we attempt to estimate the frequency of events like ours.

5 SYNTHETIC OBSERVABLES OF THE EJECTA

We map the ejecta including their detailed composition from the nucleosynthesis post-processing of 10^6 Lagrangian tracer particles to a spherical 1D mesh as well as a cylindrical 2D mesh assuming axisymmetry.

We then run the radiation transfer code SUPERNU (Wollaeger et al. 2013; Wollaeger & van Rossum 2014) in order to calculate synthetic light curves and spectra for the explosion. SUPERNU uses implicit Monte Carlo (IMC) and discrete diffusion Monte Carlo (DDMC) methods to stochastically solve the special-relativistic radiative transport and diffusion equations to first order in v/c in up to three dimensions. The hybrid IMC and DDMC scheme used in SUPERNU makes it computationally efficient in regions with high optical depth. This approach allows SUPERNU to solve for energy diffusion with very few approximations, which is very relevant for supernova light curves.

The bolometric light curves for the 1D RT model, the angle averaged light curve of the 2D RT model, as well as the light curves for three different lines of sight of the 2D RT model are shown in Fig. 7. The bolometric light curve peaks 16 d after the explosion at an absolute magnitude of $M_{\text{bol}} \approx -15$, which makes it significantly

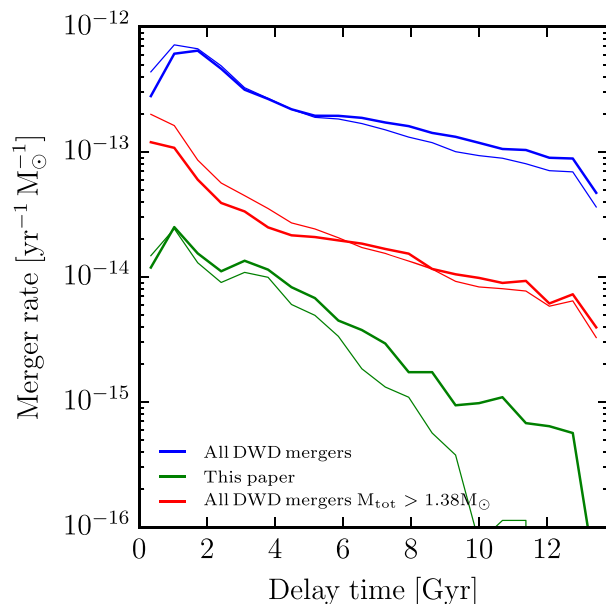


Figure 8. Merger rates for all double WD (DWD) mergers (blue), the traditional DWD merger channel for SNe Ia that assumes all merging DWD binaries with a total mass $M_{\text{tot}} > 1.38 M_{\odot}$ produce an SN Ia (red) and the scenario described in this paper (green). Thick lines use the $\gamma\alpha$ model, thin lines the $\alpha\alpha$ model for common envelope evolution.

fainter than even the faintest SNe Ia. The faintness is expected for the tiny amount of radioactive material produced.

The bolometric light curves show significant line-of-sight dependence, with a spread of about one magnitude at peak between the brightest line of sight (the negative z -axis, along the direction of the angular momentum vector of the binary system) and the faintest line of sight (the positive z -axis). Observers in the plain of rotation see a bolometric light curve that is similar to the angle averaged bolometric light curve at peak.

At late times, the angle averaged bolometric light curve is dominated by emission in the direction of the positive z -axis (which was the faintest direction at peak).

Since the ejecta contain a large amount of $2 \times 10^{-3} M_{\odot}$ of ^{44}Ti the transient will likely appear very red.

6 EVENT RATES AND BINARY EVOLUTION

In this section, we estimate the occurrence rate of explosions similar to the one described in detail above based on binary population synthesis modelling. We use the binary evolution code SeBa (Portegies Zwart & Verbunt 1996; Toonen, Nelemans & Portegies Zwart 2012) to simulate the evolution of three million binaries per model starting from the zero-age main-sequence (ZAMS) until the merger of the double WD system. At every time-step, processes such as stellar winds, mass transfer, angular momentum loss, tides, and gravitational radiation are considered with the appropriate prescriptions. SeBa is freely available through the Astrophysics MUlti-purpose Software Environment, or AMUSE (Portegies Zwart et al. 2009; Portegies Zwart & McMillan 2018, see also amusecode.org).

As the main cause for discrepancies between different binary population synthesis codes is found in the choice of input physics and initial conditions (Toonen et al. 2014), we construct two models (model $\alpha\alpha$ and $\gamma\alpha$) that are typically used in double WD modelling with SeBa (see e.g. Toonen et al. 2012; Rebassa-Mansergas et al.

2019; Zenati et al. 2019). These models differ with respect to the modelling of unstable mass transfer, i.e. common-envelope (CE) evolution (Ivanova et al. 2013). Generally the CE phase is modelled on the basis of energy conservation (Paczynski 1976; Webbink 1984). In this model, orbital energy is consumed to unbind the CE with an efficiency α_{CE} (equation B1). This recipe is used in model $\alpha\alpha$ for every CE phase. In our alternative model ($\gamma\alpha$) of CE evolution, we consider a balance of angular momentum with an efficiency parameter γ (equation B2, Nelemans et al. 2000). The γ -recipe is used unless the binary contains a compact object or the CE is triggered by a tidal instability (rather than dynamically unstable RLOF). More details on the models are given in Appendix B.

Previous work has already shown that hybrid WDs are common (Zenati et al. 2019) and frequently merge with other WDs (Perets et al. 2019). Here, we focus on mergers between a massive hybrid WD ($M_{\text{Hybrid}} \gtrsim 0.63 M_{\odot}$) and a CO WD ($M_{\text{Hybrid}} < M_{\text{CO}} \lesssim 0.85 M_{\odot}$). On average, they make up about several per cents of all double WD mergers, giving an integrated rate of several 10^{-5} events per solar mass of created stars over a Hubble time.

The typical evolution towards the merger consists of several phases of interaction. Generally the CO WD forms first, afterwards the hybrid WD is formed. This is the case for 76 per cent of the systems in our default models ($M_{\text{Hybrid}} > 0.63 M_{\odot}$, $m_{\text{CO}} < 0.85 M_{\odot}$), and 66–83 per cent with the variations as described below.

For the majority of these, the progenitor of the hybrid is initially (i.e. on the ZAMS) the more massive star in the system. Consequently, it is this star that evolves off the MS before the companion does. It fills its Roche lobe, initiates a phase of stable mass transfer, loses its hydrogen envelope, and becomes a low-mass hydrogen-poor helium-burning star (i.e. stripped star). During the mass transfer the companion has accreted a mass of $\sim 1\text{--}2 M_{\odot}$. After the mass transfer phase has ended and the companion has evolved off the MS, the companion initiates a CE phase. After the companion’s hydrogen envelope is lost from the system, the binary consists of two stripped stars. At this stage, the companion is more massive than the progenitor of the hybrid, due to the previous phase of mass accretion. Consequently, its evolutionary time-scale as a stripped star is shorter than that of the hybrid progenitor, and it becomes a CO WD first, then after that the hybrid WD is finally formed. This channel is referred to as a formation reversal channel in (Toonen et al. 2012, see their section 4.3).

In more detail, in our two models ($\gamma\alpha$ and $\alpha\alpha$), that are shown in Fig. 8, the total merger rate of double WDs is 3.1×10^{-3} and $3.2 \times 10^{-3} M_{\odot}^{-1}$, respectively. Assuming that these events only occur for systems with $M_{\text{Hybrid}} > 0.63 M_{\odot}$ and $M_{\text{CO}} < 0.85 M_{\odot}$, the synthetic event rate is $(7\text{--}8.5) \times 10^{-5} M_{\odot}^{-1}$.

The event rate is not very sensitive to the exact minimum hybrid mass and maximum CO mass. If the minimum hybrid mass to ensure a scenario as described in this paper is as high as $M_{\text{Hybrid}} > 0.68$ as is the case for our specific simulation described above, the rate slightly decreases to $(2.9\text{--}3.4) \times 10^{-5} M_{\odot}^{-1}$. If instead, the minimum hybrid mass can be as low as $M_{\text{Hybrid}} > 0.58 M_{\odot}$,¹ the rate increases somewhat to $(1.2\text{--}1.5) \times 10^{-4} M_{\odot}^{-1}$. On the other hand, if the mass of the CO WD can be as high as $0.9 M_{\odot}$ the event rates of our default models increases to $(7.8\text{--}9.4) \times 10^{-5} M_{\odot}^{-1}$ (and up to $(1.4\text{--}1.6) \times 10^{-4} M_{\odot}^{-1}$ for $M_{\text{Hybrid}} > 0.58 M_{\odot}$). When reducing the

¹We also studied a 3D model for the case of a $0.58 M_{\odot}$ hybrid, in which case, the hybrid did not detonate, but rather was disrupted later on by the primary, as we shall discuss in more detail in a future paper. It therefore provides us with a lower limit for these companion-detonation SNe.

minimum CO mass $M_{\text{CO}} < 0.8 M_{\odot}$, the event rate decreases slightly to $(6.5\text{--}7.3) \times 10^{-5} M_{\odot}^{-1}$ [and down to $(2.7\text{--}2.9) \times 10^{-5} M_{\odot}^{-1}$ for $M_{\text{Hybrid}} > 0.68 M_{\odot}$].

Overall these types of mergers comprise about 2.5 per cent of all double WD mergers in our default models, and 0.9–5.1 per cent with the variations in the limiting values of M_{Hybrid} and M_{CO} .

The event rates described above are based on stellar simulations at Solar metallicity, here taken as $Z = Z_{\odot} = 0.02$. At lower metallicities, the synthetic event rates are not significantly different. The overall rate for the default models $\gamma\alpha$ and $\alpha\alpha$ is $(9.5\text{--}9.8) \times 10^{-5} M_{\odot}^{-1}$ at $Z = 0.001$.

The event rate is about an order of magnitude lower than the estimated SNe Ia rate (Li et al. 2011; Maoz & Graur 2017). If all SNe Ia would originate from the D6 scenario, we expect to find ≈ 20 hypervelocity WDs that are surviving companion WDs of SNe Ia. However, Shen et al. (2018b) only found three candidates, inconsistent with the D6 scenario but roughly consistent with optimistic rates for our scenario. A significantly larger number of those WDs would likely make them inconsistent with a common origin from our scenario.

7 SUMMARY AND OUTLOOK

We presented a 3D hydrodynamical simulation of the final phase of a double WD binary consisting of a hybrid WD with massive $0.1 M_{\odot}$ He shell and a CO WD that are about to merge.

We find that after some initial mass transfer of helium from the secondary hybrid WD on the primary CO WD a thin helium shell builds up around the CO WD. We showed that as the accretion stream becomes denser and its impact on the surface of the CO WD becomes more violent eventually a helium detonation forms on the surface of the CO WD.

The helium detonation wraps around the CO WD but fails to ignite the CO core as the little amount of helium around the CO WD only creates a weak detonation and the shock wave from the detonation converges far off-centre in the CO WD at low densities.

However, the helium detonation also travels up the accretion stream and burns the thick helium shell around the hybrid WD. We show that this generates a strong shock wave that converges close to the centre of the CO core of the hybrid WD and ignites a carbon detonation.

The hybrid WD is completely burned and unbound by the carbon detonation. Owing to compression of the core of the hybrid WD by the strong shock wave the carbon detonation is able to synthesise $0.018 M_{\odot}$ of ^{56}Ni despite the initial low central density of the hybrid WD. The ejecta lead to a very faint and likely very red transient, that lasts for several tens of days. We estimated the event rate of the scenario described here as up to 10 per cent of the SNe Ia rate, making them an interesting target for more sensitive observations by future facilities like the Vera C. Rubin Observatory.

The CO WD remains intact and is flung at high velocity to become a hyper-velocity WD, with ejection velocity of the order of its original orbital velocity of 1300 km s^{-1} relative to the rest frame of the original binary system. It collects a thin outer layer from the ashes of the explosion of the hybrid WD that contains $5 \times 10^{-3} M_{\odot}$ of ^{56}Ni and provides an alternative origin for identified hyper-velocity WDs to the D6 model proposed by (Shen et al. 2018b). Moreover, the expected rates of such hyper-velocity WDs from our modelled scenario are consistent with the current observationally inferred rate of hyper-velocity WDs (using the GAIA catalogue; Shen et al. 2018b), which are significantly lower than suggested by the D6 model.

We expect the centre-of-mass velocity of the ejecta of the exploding (secondary) WD to also have a velocity shift of the order of 1600 km s^{-1} , in the opposite direction to that of the hyper-velocity WD, which might be observable as a systematic shift of SNE velocities compared with their host galaxies. In Galactic cases, one might find SNRs related to specific hyper-velocity WDs. In those cases the SNR, centre-of-mass velocity should be similarly high and directed in the opposite direction with that of the hyper-velocity WD.

Explosions of secondary WDs in double WD binary systems have been seen previously (Pakmor et al. 2012; Papish et al. 2015; Tanikawa et al. 2019) though always triggered by an explosion of the primary WD, that is absent in our scenario.

We conclude that detonation of hybrid WDs mediated by He detonations on primary companions generate new interesting scenarios for novel transients that need to further investigated in 3D hydrodynamical simulations, and searched for by future surveys.

ACKNOWLEDGEMENTS

RP thanks Markus Kromer, Stefan Taubenberger, Wolfgang Hillebrandt, and Sasha Kozyreva for interesting and helpful discussions. ST acknowledge support from the Netherlands Research Council NWO (VENI 639.041.645 grants). YZ and HBP thank Daan Van Rossum for interesting discussions and acknowledge support for this project from the European Union's Horizon 2020 research and innovation program under grant agreement no. 865932-ERC-SNeX.

DATA AVAILABILITY

The simulations underlying this article will be shared on reasonable request to the corresponding author.

REFERENCES

- Beuermann K., Burwitz V., Reinsch K., Schwöpe A., Thomas H. C., 2020, *A&A*, 634, A91
- Camacho J., Torres S., García-Berro E., Zorotovic M., Schreiber M. R., Rebassa-Mansergas A., Nebot Gómez-Morán A., Gänsicke B. T., 2014, *A&A*, 566, A86
- Cybur R. H. et al., 2010, *ApJS*, 189, 240
- de Kool M., van den Heuvel E. P. J., Pylyser E., 1987, *A&A*, 183, 47
- Dewi J. D. M., Tauris T. M., 2000, *A&A*, 360, 1043
- Fink M., Hillebrandt W., Röpke F. K., 2007, *A&A*, 476, 1133
- Guilloc'hon J., Dan M., Ramirez-Ruiz E., Rosswog S., 2010, *ApJ*, 709, L64
- Iben I., Jr, Tutukov A. V., 1985, *ApJS*, 58, 661
- Iben I., Jr, Nomoto K., Tornambe A., Tutukov A. V., 1987, *ApJ*, 317, 717
- Istrate A. G., Marchant P., Tauris T. M., Langer N., Stancliffe R. J., Grassitelli L., 2016, *A&A*, 595, A35
- Ivanova N. et al., 2013, *A&AR*, 21, 59
- Jacobson-Galán W. V. et al., 2020, *ApJ*, 898, 166
- Katz M. P., Zingale M., 2019, *ApJ*, 874, 169
- Kupfer T. et al., 2020, *ApJ*, 891, 45
- Kushnir D., Katz B., 2020, *MNRAS*, 493, 5413
- Kushnir D., Katz B., Dong S., Livne E., Fernández R., 2013, *ApJ*, 778, L37
- Law-Smith J. A. P. et al., 2020, preprint (arXiv:2011.06630)
- Li W., Chornock R., Leaman J., Filippenko A. V., Poznanski D., Wang X., Ganeshalingam M., Mannucci F., 2011, *MNRAS*, 412, 1473
- Livio M., Soker N., 1988, *ApJ*, 329, 764
- Loveridge A. J., van der Sluys M. V., Kalogera V., 2011, *ApJ*, 743, 49
- Maoz D., Graur O., 2017, *ApJ*, 848, 25
- Nelemans G., Verbunt F., Yungelson L. R., Portegies Zwart S. F., 2000, *A&A*, 360, 1011
- Nelemans G., Yungelson L. R., Portegies Zwart S. F., Verbunt F., 2001, *A&A*, 365, 491

- Neunteufel P., Yoon S. C., Langer N., 2016, *A&A*, 589, A43
- Neunteufel P., Yoon S. C., Langer N., 2019, *A&A*, 627, A14
- Ohlmann S. T., Röpke F. K., Pakmor R., Springel V., 2017, *A&A*, 599, A5
- Paczynski B., 1976, in Eggleton P., Mitton S., Whelan J., eds, Proc. IAU Symp. Vol. 73, Structure and Evolution of Close Binary Systems, Dordrecht, Holland ; Boston : D. Reidel Pub. Co.. p. 75
- Pakmor R., Bauer A., Springel V., 2011, *MNRAS*, 418, 1392
- Pakmor R., Edelmann P., Röpke F. K., Hillebrandt W., 2012, *MNRAS*, 424, 2222
- Pakmor R., Kromer M., Taubenberger S., Springel V., 2013, *ApJ*, 770, L8
- Pakmor R., Springel V., Bauer A., Mocz P., Muñoz D. J., Ohlmann S. T., Schaal K., Zhu C., 2016, *MNRAS*, 455, 1134
- Papish O., Soker N., García-Berro E., Aznar-Siguán G., 2015, *MNRAS*, 449, 942
- Parsons S. G. et al., 2020, *Nat. Astron.*, 4, 690
- Paxton B., Bildsten L., Dotter A., Herwig F., Lesaffre P., Timmes F., 2011, *ApJS*, 192, 3
- Paxton B. et al., 2019, *ApJS*, 243, 10
- Perets H. B., Zenati Y., Toonen S., Bobrick A., 2019, preprint (arXiv:1910.07532)
- Portegies Zwart S., 2013, *MNRAS*, 429, L45
- Portegies Zwart S., McMillan S., 2018, *Astrophysical Recipes: The Art of AMUSE*, Iop Publishing Ltd.
- Portegies Zwart S. F., Verbunt F., 1996, *A&A*, 309, 179
- Portegies Zwart S. et al., 2009, *New Astron.*, 14, 369
- Prada Moroni P. G., Straniero O., 2009, *A&A*, 507, 1575
- Rebassa-Mansergas A., Toonen S., Korol V., Torres S., 2019, *MNRAS*, 482, 3656
- Ruiter A. J., Belczynski K., Sim S. A., Seitzzahl I. R., Kwiatkowski D., 2014, *MNRAS*, 440, L101
- Sato Y., Nakasato N., Tanikawa A., Nomoto K., Maeda K., Hachisu I., 2015, *ApJ*, 807, 105
- Seitzzahl I. R., Meakin C. A., Townsley D. M., Lamb D. Q., Truran J. W., 2009, *ApJ*, 696, 515
- Shen K. J., Bildsten L., 2014, *ApJ*, 785, 61
- Shen K. J., Moore K., 2014, *ApJ*, 797, 46
- Shen K. J., Kasen D., Miles B. J., Townsley D. M., 2018a, *ApJ*, 854, 52
- Shen K. J. et al., 2018b, *ApJ*, 865, 15
- Sim S. A., Röpke F. K., Hillebrandt W., Kromer M., Pakmor R., Fink M., Ruiter A. J., Seitzzahl I. R., 2010, *ApJ*, 714, L52
- Springel V., 2010, *MNRAS*, 401, 791
- Tanikawa A., Nomoto K., Nakasato N., Maeda K., 2019, *ApJ*, 885, 103
- Timmes F. X., Swesty F. D., 2000, *ApJS*, 126, 501
- Toonen S., Nelemans G., 2013, *A&A*, 557, A87
- Toonen S., Nelemans G., Portegies Zwart S., 2012, *A&A*, 546, A70
- Toonen S., Claeys J. S. W., Mennekens N., Ruiter A. J., 2014, *A&A*, 562, A14
- Toonen S., Hollands M., Gänsicke B. T., Boekholt T., 2017, *A&A*, 602, A16
- Tutukov A. V., Yungelson L. R., 1992, *SvA*, 36, 266
- Webbink R. F., 1984, *ApJ*, 277, 355
- Weinberger R., Springel V., Pakmor R., 2020, *ApJS*, 248, 32
- Wollaeger R. T., van Rossum D. R., 2014, *ApJS*, 214, 28
- Wollaeger R. T., van Rossum D. R., Graziani C., Couch S. M., Jordan G. C. IV, Lamb D. Q., Moses G. A., 2013, *ApJS*, 209, 36
- Xu X.-J., Li X.-D., 2010, *ApJ*, 716, 114
- Zenati Y., Toonen S., Perets H. B., 2019, *MNRAS*, 482, 1135
- Zhang X., Hall P. D., Jeffery C. S., Bi S., 2018, *MNRAS*, 474, 427
- Zorotovic M., Schreiber M. R., Gänsicke B. T., Nebot Gómez-Morán A., 2010, *A&A*, 520, A86

APPENDIX A: NUCLEAR BURNING LIMITER

Recently, it has been discussed that the nuclear burning limiter that is needed in 3D simulations of thermonuclear explosions because detonations are fundamentally unresolved can make a difference for yields of the nuclear burning (Kushnir et al. 2013; Shen et al. 2018a; Katz & Zingale 2019; Kushnir & Katz 2020).

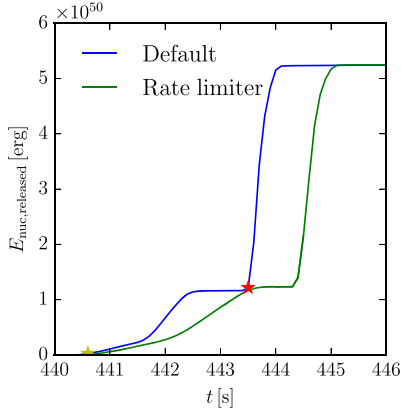


Figure A1. Nuclear energy release with time for the default simulation (blue) discussed in the main paper and an otherwise identical simulation using an additional limiter for the nuclear burning that reduces nuclear reaction rates (green). The yellow and red star denote the times when the helium and carbon detonations ignite for the default simulation.

To better understand the differences between limiters as well as to improve our confidence in our results, we have repeated the merger simulation in AREPO until nuclear burning ceases with a limiter on the nuclear reaction rates (Kushnir et al. 2013).

As described in the main text, in our default configuration we attempt to detect the cells directly behind the shock of the detonation and disable nuclear burning in them. In practice, we disable nuclear burning for cells that fulfill $\nabla \cdot \vec{v} < 0$ and $|\nabla P|_{\text{cell}}/P > 0.66$.

In our rerun, we dynamically reduce all nuclear reaction rates in a cell by a constant factor such that $\Delta \ln T \leq 0.1$ in every time-step. This ensures that the nuclear time-scale is always longer than the hydrodynamical time-scale of a cell.

We show the time evolution of the nuclear energy release of the standard simulation (the same as in the lower panel, Fig. 1) and the rerun with the additional reaction rate limiter in Fig. A1. Both simulations show qualitatively the same evolution.

As shown in Fig. A2, they both ignite a helium detonation at the same time and place on the surface of the CO WD. Moreover, in both simulations the helium detonation ignites a carbon detonation only in the hybrid WD. The total nuclear energy release of the helium detonation as well as the carbon detonation is essentially identical. Thus, we conclude that our main results are independent of the details of the nuclear burning limiter.

The main difference is the speed of the energy release during the helium detonation. In the simulation with the additional rate limiter, the nuclear reactions are significantly slowed down, so that the helium detonation releases its energy more slowly. This also slows down the propagation of the helium detonation and the carbon detonation is ignited about 1 s later compared to our standard simulation without the rate limiter. The difference is much smaller for the carbon detonation, though it is also slowed down a little bit by the rate limiter. Nevertheless, the final yields and total energy release are the same for either limiter making us confident that our results are at least qualitatively stable.

APPENDIX B: COMMON-ENVELOPE PHASE

In this study, we simulate the effect of the CE phase in two ways (Section 6); based on energy conservation (Paczynski 1976; Webbink

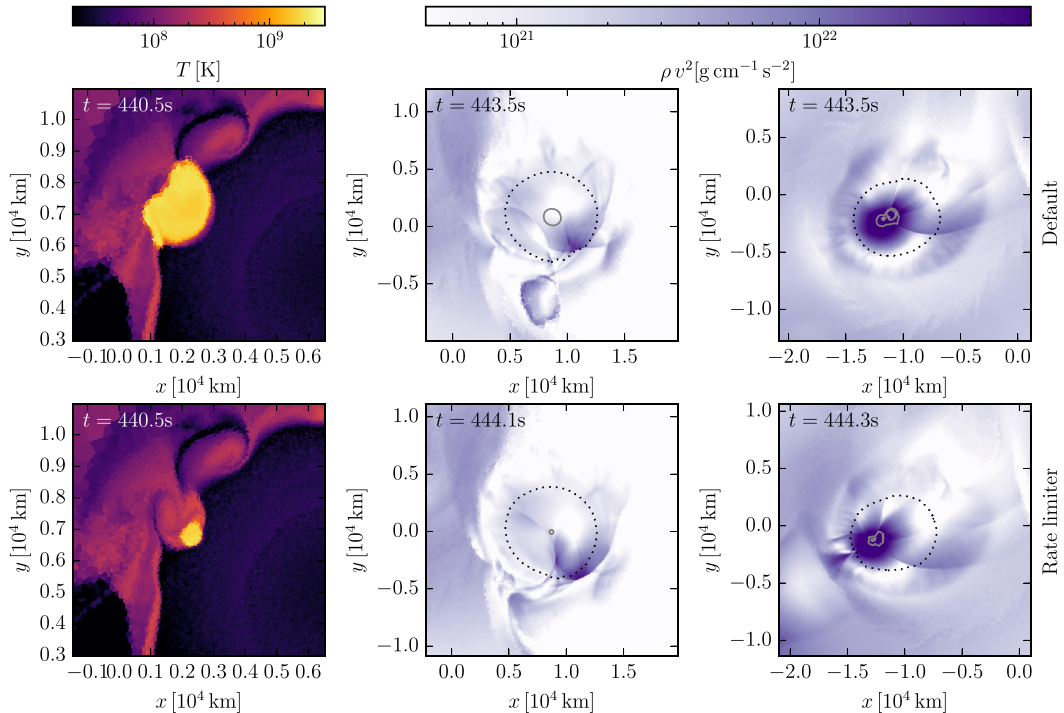


Figure A2. Comparison of the ignition of the helium detonation and the convergence of the shock fronts in both WDs of the default simulation (top row) with an otherwise identical simulation using an additional limiter for the nuclear burning that reduces nuclear reaction rates (bottom row). The left-hand panel shows the temperature around the ignition point of the helium detonation 0.1 s after ignition. The middle and right-hand panels show the primary and secondary WD, respectively, at the times when the shockwaves that originate from the helium detonation converge in their CO core.

1984) or a balance of angular momentum (Nelemans et al. 2000). In the former model, orbital energy is consumed to unbind the CE with an efficiency α_{CE} :

$$E_{\text{bin}} = \frac{GM_{\text{d}}M_{\text{c}}}{\lambda R} = \alpha_{\text{CE}}E_{\text{orbit}}, \quad (\text{B1})$$

where E_{bin} is the binding energy of the envelope, M_{d} is the mass of the donor star, M_{c} the mass of its core, R its radius, and E_{orbit} the orbital energy of the binary at the onset of the CE phase. λ the structure parameter of its envelope (de Kool, van den Heuvel & Pylyser 1987; Livio & Soker 1988; Dewi & Tauris 2000; Xu & Li 2010; Loveridge, van der Sluys & Kalogera 2011). In the model $\alpha\alpha$, we assume $\alpha_{\text{CE}}\lambda = 2$. This is calibrated to the formation of double WDs (i.e. second phase of mass transfer, see Nelemans et al. 2000, 2001; Toonen et al. 2012).

In the latter model, the γ -parameter describes the efficiency with which orbital angular momentum is used to expel the CE according to

$$\frac{J_{\text{b,init}} - J_{\text{b,final}}}{J_{\text{b,init}}} = \gamma \frac{\Delta M_{\text{d}}}{M_{\text{d}} + M_{\text{a}}}, \quad (\text{B2})$$

where $J_{\text{b,init}}$ and $J_{\text{b,final}}$ are the orbital angular momentum of the pre- and post-mass transfer binary respectively, and M_{a} is the mass of the companion. The motivation for the γ -formalism comes from observed double WD systems. The first phase of mass transfer in the evolution to form a double WD could not be explained by the α -formalism nor stable mass transfer for a Hertzsprung gap donor star (see Nelemans et al. 2000). Here, we assume $\gamma = 1.75$, which

is calibrated to the mass-ratio distribution of observed double WDs (Nelemans et al. 2001; Toonen et al. 2012).

Other constraints on CE evolution exist which are based on other types of binaries. For example, from the demographics of the observed population of compact WD–M dwarf systems (often called post-common envelope binaries) a small value of $\alpha_{\text{CE}}\lambda$ (≈ 0.25) is derived (Zorotovic et al. 2010; Portegies Zwart 2013; Toonen & Nelemans 2013; Camacho et al. 2014). Recently the hydro-dynamical simulation of Law-Smith et al. (2020) achieved a successful CE ejection and a measurable CE efficiency of $\alpha_{\text{CE}} \approx 0.1$ –0.4 for a CE initiated by a $12 M_{\odot}$ supergiant with a neutron-star companion. However, in the context of double WDs, modelling each CE-phase with such a small value of $\alpha_{\text{CE}}\lambda$, leads to a mass ratio distribution that is at odds with the observed population, see e.g. Nelemans et al. (2000) and Toonen et al. (2017, their model $\alpha\alpha 2$).

Additionally, we note that the synthetic double WD space density from both our models $\alpha\alpha$ and $\gamma\alpha$ is in agreement with the observed range (Rebassa-Mansergas et al. 2019, see their discussion, section 6.2). Despite the uncertainties in binary population synthesis modelling in general, and the CE phase in particular, the match in space densities provides confidence in the synthetic double WD merger rates provided in this paper, especially for model $\gamma\alpha$ that also reproduces the observed mass ratio distribution of double white dwarfs.

This paper has been typeset from a $\text{\TeX/L\AA}\text{\TeX}$ file prepared by the author.